Tumor-immune metaphenotypes orchestrate an evolutionary bottleneck that promotes metabolic transformation

Jeffrey West[1,*], Frederika Rentzeperis[2], Casey Adam[3], Rafael Bravo[1], Kimberly A. Luddy[4], Mark Robertson-Tessi[1], and Alexander R. A. Anderson[1,+]

[1]Integrated Mathematical Oncology Department, H. Lee Moffitt Cancer Center & Research Institute, 12902 Magnolia Drive, SRB 4 Rm 24000H Tampa, Florida, 33612
[2]Icahn School of Medicine at Mount Sinai, New York, NY, 10029
[3]Department of Engineering Science, University of Oxford, Oxford
[4]Cancer Biology and Evolution Program, H. Lee Moffitt Cancer Center & Research Institute, Tampa, Florida
[*]jeffrey.west@moffitt.org
[+]Alexander.Anderson@moffitt.org

Abstract

Background: Metabolism plays a complex role in the evolution of cancerous tumors, including inducing a multifaceted effect on the immune system to aid immune escape. Immune escape is, by definition, a collective phenomenon by requiring the presence of two cell types interacting in close proximity: tumor and immune. The microenvironmental context of these interactions is influenced by the dynamic process of blood vessel growth and remodelling, creating heterogeneous patches of well-vascularized tumor or acidic niches.

Methods: Here, we present a multiscale mathematical model that captures the phenotypic, vascular, microenvironmental, and spatial heterogeneity which shapes acid-mediated invasion and immune escape over a biologically-realistic time scale. The model explores several immune escape mechanisms such as i) acid inactivation of immune cells, ii) competition for glucose, and iii) inhibitory immune checkpoint receptor expression (PD-L1). We also explore the efficacy of anti-PD-L1 and sodium bicarbonate buffer agents for treatment. To aid in understanding immune escape as a collective cellular phenomenon, we define immune escape in the context of six collective phenotypes (termed "meta-phenotypes"): **Self-Acidify**, **Mooch Acid**, **PD-L1 Attack**, **Mooch PD-L1**, **Proliferate Fast**, and **Starve Glucose**.

Results: Fomenting a stronger immune response leads to initial benefits (additional cytotoxicity), but this advantage is offset by increased cell turnover that leads to accelerated evolution and the emergence of aggressive phenotypes. This creates a bimodal therapy landscape: either the immune system should be maximized for complete cure, or kept in check to avoid rapid evolution of invasive cells. These constraints are dependent on heterogeneity in vascular context, microenvironmental acidification, and the strength of immune response.

Conclusions: This model helps to untangle the key constraints on evolutionary costs and benefits of three key phenotypic axes on tumor invasion and treatment: acid-resistance, glycolysis, and PD-L1 expression. The benefits of concomitant anti-PD-L1 and buffer treatments is a promising treatment strategy to limit the adverse effects of immune escape.

1 Introduction

Metabolism plays a complex but key role in the evolution of cancerous tumors. Localized hypoxia due to vascular instability and dysfunction leads to acidification of the tumor microenvironment via the Pasteur effect. Decreased pH selects for acid-resistant tumor-cell phenotypes, followed by the emergence of aerobic glycolysis (i.e., the Warburg effect[1]). The further acidification of the surrounding microenvironment by these metabolically aggressive cells foments acid-mediated invasion[2–4]. This nonlinear evolutionary trajectory through a range of metabolic phenotypes has been studied clinically, experimentally,

and theoretically[5–10]. We present an extension of a hybrid multiscale agent-based mathematical model[8] that incorporates phenotypic, vascular, microenvironmental, and spatial heterogeneity to investigate acid-mediated invasion over a biologically-realistic temporal scale, constructed in Hybrid Automata Framework (HAL)[11]. Here, we model immune predation by T cells in the metabolically altered tumor microenvironment. We include several immune escape mechanisms such as acid-mediated inactivation of T-cell activation, T-cell inhibition by checkpoint ligand expression on tumor cells, and T-cell glucose deprivation.

1.1 Metabolism and the tumor-immune response

The effect of metabolic processes on the immune system is multifaceted and complex, involving both intracellular metabolism of many varied cell types and the impact of this metabolic activity on the surrounding microenvironment. Immunometabolism is a growing area of study[12] and systems biology and modeling approaches are being applied to the field[13]. However, the dynamics of tumor-immune interactions in the context of altered cellular metabolism remain only partially understood. In this work, we focus on T cells, in particular cytotoxic T lymphocytes (CTL, also known as / CD8+ effector T cells), which are key players in the adaptive immune response to foreign pathogens and defective host cells. CTLs are activated via antigen presentation during the body's initial inflammatory response, after which they rapidly proliferate. Mathematical models are highly suited to studying tumor-immune dynamics[14–20], whether using non-spatial continuum approaches (recently reviewed in 21) or spatial agent-based models (recently reviewed in 22). However, very few tumor-immune models to date have incorporated the effects of cancer metabolism on immune function[23,24]. Here, we investigate several key connections between tumor metabolism and immune function. The physiological role of acidic niches in lymph nodes to regulate T-cell activation has been demonstrated recently[25], thus in the model here, CTLs are subject to inactivation in acidic microenvironments (see figure 5D). One recent study demonstrated that acidic microenvironments result in inactivation of CTLs but do not affect their viability[26]. Cells rescued from low pH environments had the ability to regain effector function. Tumor acidity also promotes regulatory T-cell (Tregs) activity as well as an increase of PD-1 expression on Tregs, indicating that PD-1 blockade may increase suppressive capacity[27]. Tumor-infiltrating CD8+ T-cells require glucose to support their killing function, hence compete for glucose with cancer cells (see figure 5E) dampens their anti-cancer response[28]. In contrast, Tregs avoid competition for glucose within the tumor microenvironment through rewired metabolism away from aerobic glycolysis, which enhances their immune-suppression function within the tumor[29].

We also include checkpoint inhibition in our model. Programmed cell death-1 (PD-1) is an inhibitory immune checkpoint receptor expressed on activated CTLs, and programmed cell death ligand-1 (PD-L1) is a cell surface marker typically expressed on non-hematopoietic tissues that activates PD-1 signaling[30]. Upon PD-L1 binding to PD-1, antigen-specific T-cells undergo inactivation and apoptosis[31] and suppressive T-cells become more prominent[32], thereby down-regulating the immune system response. Some cancers constitutively express PD-L1, thereby making them less visible to the immune system. This mechanism is targetable with anti-PD-1/PD-L1 therapy. In the event that a tumor develops escape or evasion mechanisms in response to immune attack, selection may occur for subclonal populations capable of withstanding immune predation[33,34], often well before tumor invasion into normal tissue[35]. Classifying tumors into immune-hot or -cold has shown both intra- and inter-tumoral heterogeneity based on immune infiltration[36,37].

Immunotherapies targeting checkpoint pathways are effective in multiple cancer types, however many patients remain unresponsive or eventually recur due to an immuno-suppressive tumor microenvironment. Combining oral bicarbonate buffering with immunotherapy (adoptive T-cell transfer, anti-CTLA4, or anti PD-1) increased responses in murine cancer models, presumably due to increased immune activity in a less acidic microenvironment[26]. Below, we extend a mathematical model of cancer metabolism[8–10] by incorporating immune predation (T cells) to investigate optimal strategies for immunotherapy (anti-PD-L1) and bicarbonate buffer therapy.

1.2 Dynamic vasculature may create acidic niches

Blood vessel growth and remodelling is a dynamic process, responding to stimuli from cells in the nearby tissue, signaling factors within microenvironmental context, and treatment[38]. These vascular dynamics are often abnormal in tumors, and areas of poor vascularization are prone to develop acidic niches. Mechanistic modeling has been used to investigate the treatment effects of systemic pH buffers (sodium bicarbonate) to limit microenvironmental selection for acid-adapted phenotypes arising in such niches, and this approach

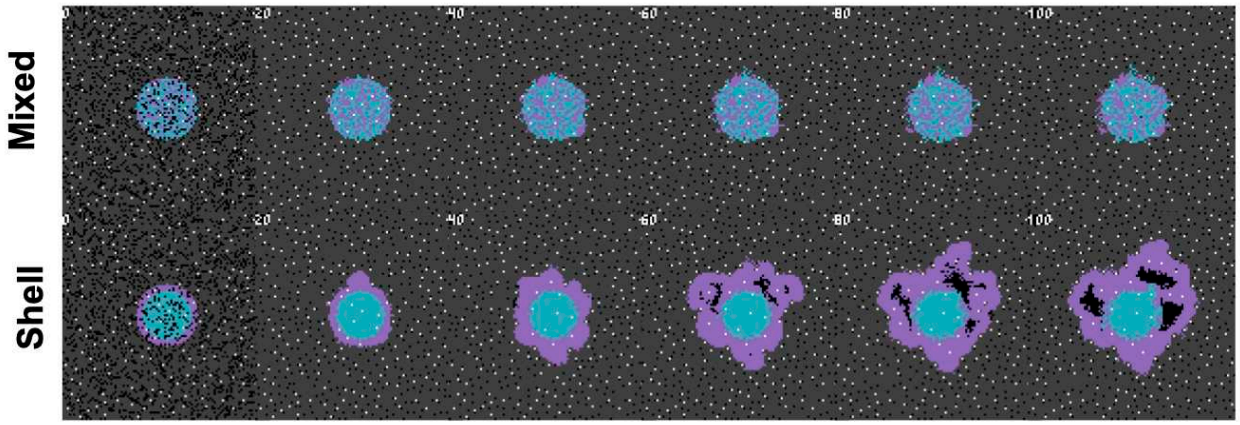

Figure 1. Collective phenotypes drive acid-mediated invasion. Spatial and temporal evolution of two distinct initial spatial configurations of identical numbers of cellular phenotypes leads to differential outcomes due to context-dependent selection. A low glycolysis phenotype (blue) and a high glycolysis phenotype (purple) compete for resources according to the rules outlined in Box 1 (see Methods). Top row: a mixed configuration leads to no evolution. Acid-mediated invasion does not occur because the volumetric concentration of acid produced by aggressive cells is not enough to cause invasion when highly glycolytic cells are seeded far apart. Bottom row: In contrast, artificially placing the aggressive high glycolysis phenotypes on the rim leads to invasion from increased volumetric acid via a group-effect.

can significantly delay carcinogenesis in TRAMP mice[9,39]. Buffers reduce intratumoral and peritumoral acidosis, inhibiting tumor growth[6] and reducing spontaneous and experimental metastases[40,41]. Here, we model T-cell recruitment through the vasculature with subsequent migration into the surrounding tumor, and this leads to an uneven distribution of immune-mediated kill due to pockets of immune-protected acidic niches. The complex interplay between immune, normal, and cancer cells with varied individual phenotypes each within a specific environmental context results in dynamic spatial and temporal variation that is greater than the sum of the individual parts. This necessitates mathematical modeling approaches that account for each hierarchical scale of the system[42].

A patient's homeostatic healthy ecosystem can influence the emergent evolutionary dynamics in cancer progression and treatment[43], dependent upon factors such as the tissue architecture at tumor initiation[44], surrounding stroma[45], and negative selection imposed by immune response[46–48]. To address the interplay between normal homeostatic well-vascularized tissue, immune response, and cancer progression and treatment we construct and interrogate a hybrid discrete continuous model[8]. The model accounts for evolving metabolic phenotypes, vasculature, immune response, microenvironmental conditions, and immune escape mechanisms.

1.3 Collective cellular phenotypes: the "Metaphenotype"

The model introduced here is an extension of previous modeling work[8–10], by including immune predation and immunotherapy. Figure 2 illustrates the behavior of cells interacting with neighbors and environmental factors (panel A), the rules governing internal tumor cell decisions (panel B), the range of phenotype space (acid resistance, glycolysis, and PD-L1 in panel C), and the rules governing T-cell internal decision (panel D).

Previously published iterations of the model noted that the individual cellular phenotype was insufficient to define behaviors such as acid-mediated invasion[8], but did not attempt to quantify any collective phenotypic behavior. A simple, contrived example in figure 1 illustrates the need to quantify context-dependent selection in this model. This figure shows the time-evolution of identical phenotypic compositions that have varied initial spatial configurations (mixed or shell). The mixed configuration of low glycolysis (blue) and high glycolysis (purple) phenotypes leads to no evolution. The volumetric concentration of acid produced by aggressive cells is not enough to cause invasion when highly glycolytic cells are seeded far apart. In contrast, artificially placing the aggressive high glycolysis phenotypes on the rim leads to invasion from increased volumetric acid via a group-effect. Clearly, both the phenotype and neighboring context is important.

In order to describe the collective nature of phenotypes operating within the context of surrounding cells

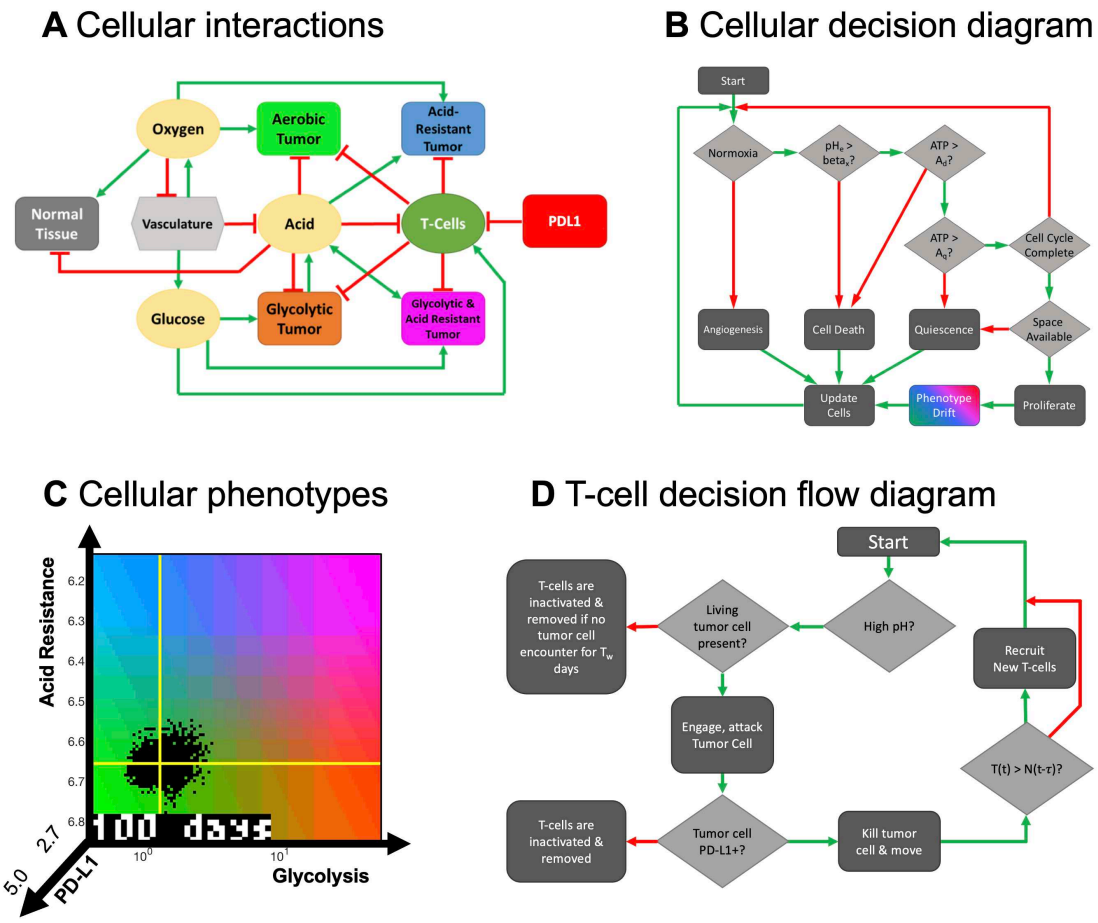

Figure 2. Hybrid Discrete-Continuum Model Diagram. (A) Model interaction network for diffusible molecules (yellow), vasculature (light gray), normal tissue (dark gray), and variable tumor phenotypes (colors). Red lines indicate inhibitory interactions while green lines indicated promoting interactions. (B) Decision process for each cell, with diamonds representing decisions. Green arrows indicate that the condition is satisfied, and red that the condition is not met. (C) A map of tumor phenotype state space on three axes. The horizontal axis is the constitutively activated glycolytic capacity (p_G), and vertical axis is the change in acid resistance (p_H) from normal, with higher resistance to acidic conditions being higher on the plot, and the final axis is constitutively expressed PD-L1 (p_P). The normal metabolic phenotype is at the intersection of the two yellow lines, with the cloud of black dots representing normal variation in phenotypes within the tumor composition (each black dot is a single tumor cell). (D) Decision process for T-cells. T-cells are recruited in proportion to tumor size at a rate of α_T. T-cells are inactivated and removed if they remain is acidic conditions too long, or if they are inactivated by a PD-L1 positive cancer cell.

and environmental conditions, we propose the concept of a "metaphenotype". Each of these metaphenotypes account for phenotypic traits (e.g. PD-L1 expression) as well as surrounding environmental context (e.g. local glucose or pH concentration), and competition with neighboring cell types (immune, cancer, normal).

1.4 The tumor-immune gambit

Recently, mathematical models have focused on the role of "immuno-architecture" to predict the effect of tumor-immune interactions on survival and response to immune checkpoint inhibitors[49–51]. A recent study in triple-negative breast cancer classified immunohistochemistry images into three spatial immunophenotypes: excluded (T-cells at the tumor border), ignored (negligible T-cell presence), and inflamed (evenly distributed T-cell presence)[49]. Ignored and excluded phenotypes are prognostic of poor survival and resistance to anti-PD-L1 treatment. Another study introduced a three-dimensional multi-scale agent-based modeling approach where effector and cytotoxic T-cells are recruited through spatially heterogeneous vasculature[50]. The authors proposed a prognostic score of the fraction of PD-L1-expressing cells within the tumor rim. Interestingly, the

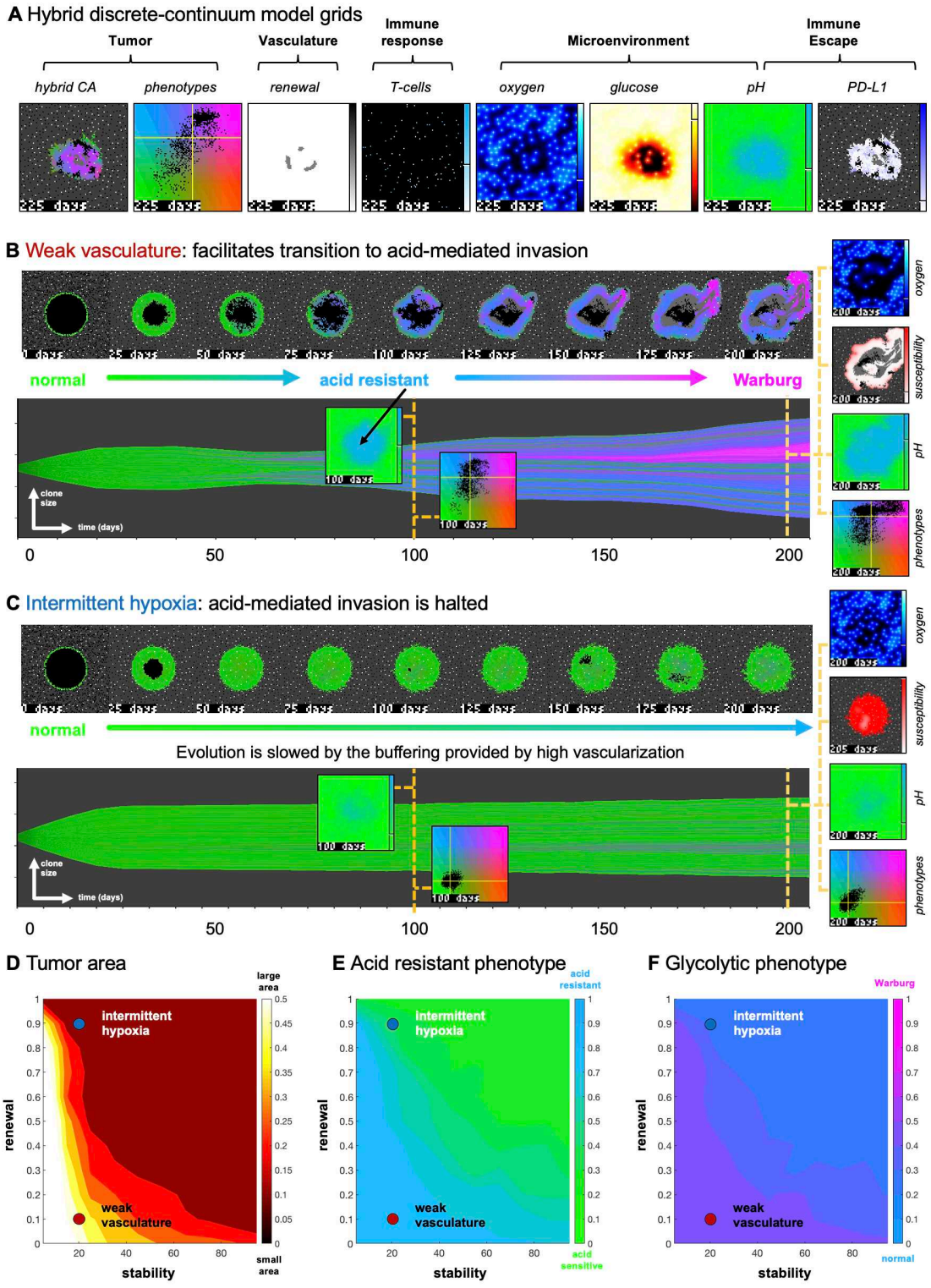

Figure 3. The effect of vasculature renewal and stability on tumor size and phenotype. (A) Snapshot (at 225 days) is shown for the full multi-scale hybrid cellular automata model: tumor spatial map, phenotypes, vascular renewal probability, T-cells, diffusible molecules (oxygen, glucose, pH), tumor cell PD-L1, and immune susceptibility (see equation 12). Each snapshot has corresponding colorbar (right) with marker indicating average value. (B) An example realization of "weak vasculature" ($\nu_{mean} = 20; p_{ang} = 0.1$). Acidic conditions in tumor core select for acid resistant and glycolytic Warburg phenotype. (C) An example realization of "intermittent hypoxia" ($\nu_{mean} = 20; p_{ang} = 0.9$), where selection is limited because of adequate vascularization within the tumor core. (D,E,F) $N = 10$ stochastic realizations are simulated, and the average tumor area (D), acid resistance phenotype (E), and glycolytic phenotype (F) across 10 values of stability ($\nu_{mean} \in [0, 100]$ days), and 10 values of renewal ($p_{ang} \in [0, 1]$). See associated supplemental video S1.

model predicted insensitivity to T-cell entry point via vascularization (e.g. core versus rim) on pre-treatment size and PD-L1 expression, but did not take into account vascular effects on oxygen, nutrients, and drug delivery. One recent work combined a hybrid model with PET imaging data to study the reshaping of metabolic activity in tumors over time[52]. High metabolic activity on the tumor periphery resulted in worse prognostic outcomes.

The back and forth of cancer treatment and a tumor's evolutionary response has often been compared to a chess match[53–55]. In this manuscript, we show that immune predation of tumors can be likened to an "immune gambit", where a temporary sacrifice of (normal glycolytic) cells on the periphery leads to long-term acceleration of the invasion of aggressive (highly glycolytic) phenotypes into surrounding tissue. This result only becomes clear when comparing to the baseline tumor metabolic evolution without immune predation. We show that poor vascularization (without immune) selects for aggressive phenotypes while high vascularization undergoes low levels of evolution. This phenomena has a Goldilocks effect, which occurs only under moderate levels of immune response. The immune gambit is described as a collective phenotype, which critically depends on the interplay between local vascularization, immune infiltration, and immune evasive phenotypes (PD-L1). A mathematical model is the ideal testing ground for this hypothesis because of direct comparison of immune predation to simulations without the presence of T-cells.

In the next section, we introduce the model, simulate baseline outcomes without immune predation (figure 3), and illustrate the immune-induced evolutionary bottleneck (figure 4). To quantify immune escape through the lens of collective phenotypes, we classify cells into six "meta" (or collective) phenotypes: **Self-Acidify**, **Mooch Acid**, **PD-L1 Attack**, **Mooch PD-L1**, **Proliferate Fast**, and **Starve Glucose**. Each metaphenotype is contingent on a recent tumor-immune interaction and defined in the context of local microenvironment, with the exception of a "null" metaphenotype: **Immune Desert**. We quantify the evolution of metaphenotypes over time, illustrating the explanatory power of collective phenotypes in describing response to buffer therapy and anti-PD-L1 in mono- and combination therapy (figure 6).

2 Results

2.1 The effect of vasculature renewal and stability on tumor size and phenotype

Figure 3A shows the complex, multi-scale hybrid CA with a snapshot (shown left-to-right) of the tumor spatial map, phenotypes, likelihood of vascular renewal, T-cells, diffusible molecules (oxygen, glucose, acid), PD-L1 and immune susceptibility. In previous versions of this model, two phenotypic axes are considered (see Methods): acid-resistance (light blue) and glycolytic (pink). Simulations are shown in the absence of immune predation to establish baseline dynamics, before quantifying immune predation in the next section.

In the middle panels of figure 3 we compare two classifications of vasculature: weak vasculature (associated with low vessel stability and low rates of vessel renewal) and intermittent hypoxia (associated with low stability, but high renewal). The spatial map of phenotypes is shown over time, along with a visualization called "phenotypic barcoding", which visualizes the clone size, phenotype and lineage information over time[10] using the EvoFreq R package[56] (for more information on interpreting phenotypic barcoding plots, see figure S4). Figure 3B depicts the process by which weak vasculature selects for aggressive tumor growth. Acidic conditions in the tumor core (low glucose, low oxygen, and high pH) cause rapid death of glycolytically normal tumor cells with low levels of acid resistance. Selection for acid resistance occurs first (blue phenotypes), followed by selection for highly glycolytic tumor cells (pink phenotypes) which eventually invade into surrounding tissue. Conversely, in figure 3C, intermittent hypoxia conditions result in little selection. The well-vascularized tumor core limits selection for aggressive phenotypes. This result underscores the importance of understanding the baseline vascular conditions before modeling the complex dynamics with the additional immune predation. A snapshot of the intratumoral oxygen, immune susceptibility (see equation 12), phenotypes, and pH is shown at the end of each simulation.

The bottom row shows the average tumor area (D), and tumor phenotypes (E,F) for simulations across a range of vascular settings (no immune). Weak vasculature typically results in larger tumors, more acid resistant phenotypes, and highly glycolytic phenotypes. Weak vasculature induces an acidic niche in the tumor core, selecting for acid-resistant phenotypes (blue). Increased turnover enables increased evolution and selection for aggressive Warburg phenotypes (pink), leading to acid-mediated invasion into surrounding normal tissue. Intermittent hypoxia (low vascular stability with high rates of renewal) generally leads to lower rates of selection and subsequently less invasion (figure 3C).

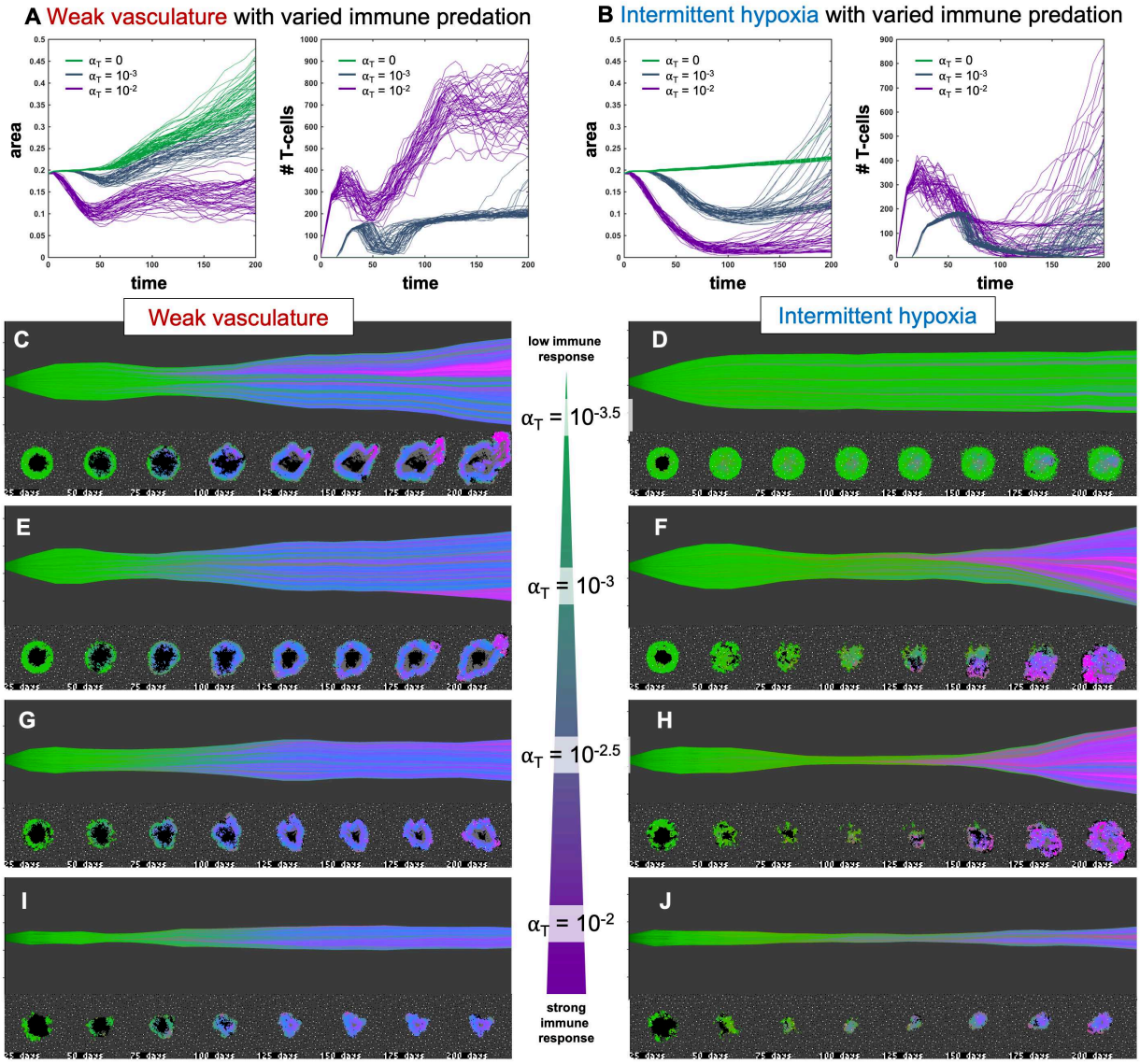

Figure 4. Immune predation induces an evolutionary bottleneck. (A,B) Tumor area over time (left) and the number of T-cells for weak vasculature (A) and intermittent hypoxia (B) conditions), shown for no T-cells (green; $\alpha_T = 0$), medium (blue-gray; $\alpha_T = 10^{-3}$) and high (purple; $\alpha_T = 10^{-2}$) immune response rates. (C-J) Example simulation stochastic realizations are shown across a range of immune response from low (top) to high (bottom). Immune predation tends to suppress tumor growth in weak vasculature conditions. In contrast, immune predation induces an evolutionary bottleneck for medium immune response rates (e.g. see F, H), causing aggressive tumor growth compared to the baseline of no immune response.

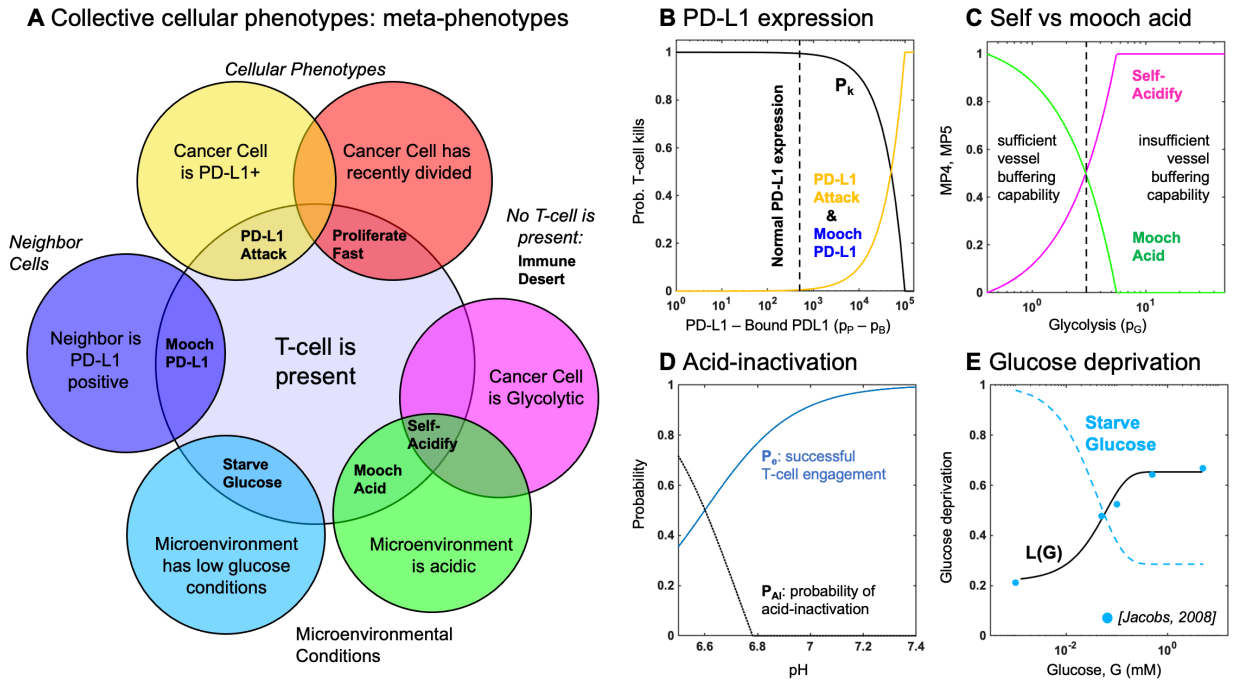

Figure 5. Defining metaphenotypes in the context of immune escape. (A) Six collective cellular metaphenotypes are defined as cancer cells with a given phenotype (e.g. PD-L1), microenvironmental condition (e.g. high acid or low glucose), or neighboring cell. Immune desert is the absence of recent immune interaction. (B) PD-L1 metaphenotypes depend on the likelihood of T-cell kill as a function of PD-L1 expression of self (**PD-L1 Attack**) or neighbor (**Mooch PD-L1**). (C) Acidification metaphenotypes depend on the rate of acidification contributed by self (**Self-Acidify**) or neighbors (**Mooch acid**). (D) The rate of acid-inactivation of T-cells. (E) Data from ref. 57 (blue dots) was used to parameterize T-cell death rate in low glucose, shown in eqn. 11. The **Starve Glucose** metaphenotype expression corresponds to low glucose concentrations.

2.2 Immune predation induces an evolutionary bottleneck

Figure 4 shows the response of two vascular conditions (weak and intermittent hypoxia) under no immune response (green; $\alpha_T = 0$), medium (blue-gray; $\alpha_T = 10^{-3}$) and high (purple; $\alpha_T = 10^{-2}$) immune response rates. Immune cells are recruited in proportion to tumor size and response rate, α_T.

Immune response tends to suppress tumor growth in weak vasculature conditions. Compared to baseline tumor growth, all levels of immune response result in greater tumor suppression. In contrast, immune predation in intermittent hypoxia conditions often leads to an initial response but fast regrowth (figure 4B, left). This is confirmed by visual inspection of the phenotypic barcoding visualizations in figure 4C-J. Weak vascular conditions select for aggressive phenotypes with little-to-no immune presence (figure 4C). The addition of immune cells only serves to slow an already aggressive tumor (figure 4E,G,I). In stark contrast, intermittent hypoxia conditions rarely select for strong growth in the absence of immune predation (figure 4D). Immune predation serves as a selection pressure, in conditions where there would otherwise be very little selection.

Immune predation under intermittent hypoxia conditions induces an evolutionary bottleneck for medium immune response rates (e.g. see F, H), causing fast selection for aggressive growth compared to the baseline of no immune response. Interestingly, this effect occurs on a "Goldilocks" scale. The long neck of the bottleneck is associated with higher rates of tumor turnover (due to immune attack), selecting for phenotypes which are 1) inside an immune-evasive niche or 2) rapidly divide to outgrow immune kill.

2.3 Metaphenotypes explain immune escape under treatment

In figure 6, we consider two treatments to mitigate immune escape and to reduce tumor growth: anti-PD-L1 (red) and a pH buffer (blue), given in isolation or combination (purple). A short window of treatment is simulated and results are compared to the untreated baseline. As seen in figure figure 6A-D, combination

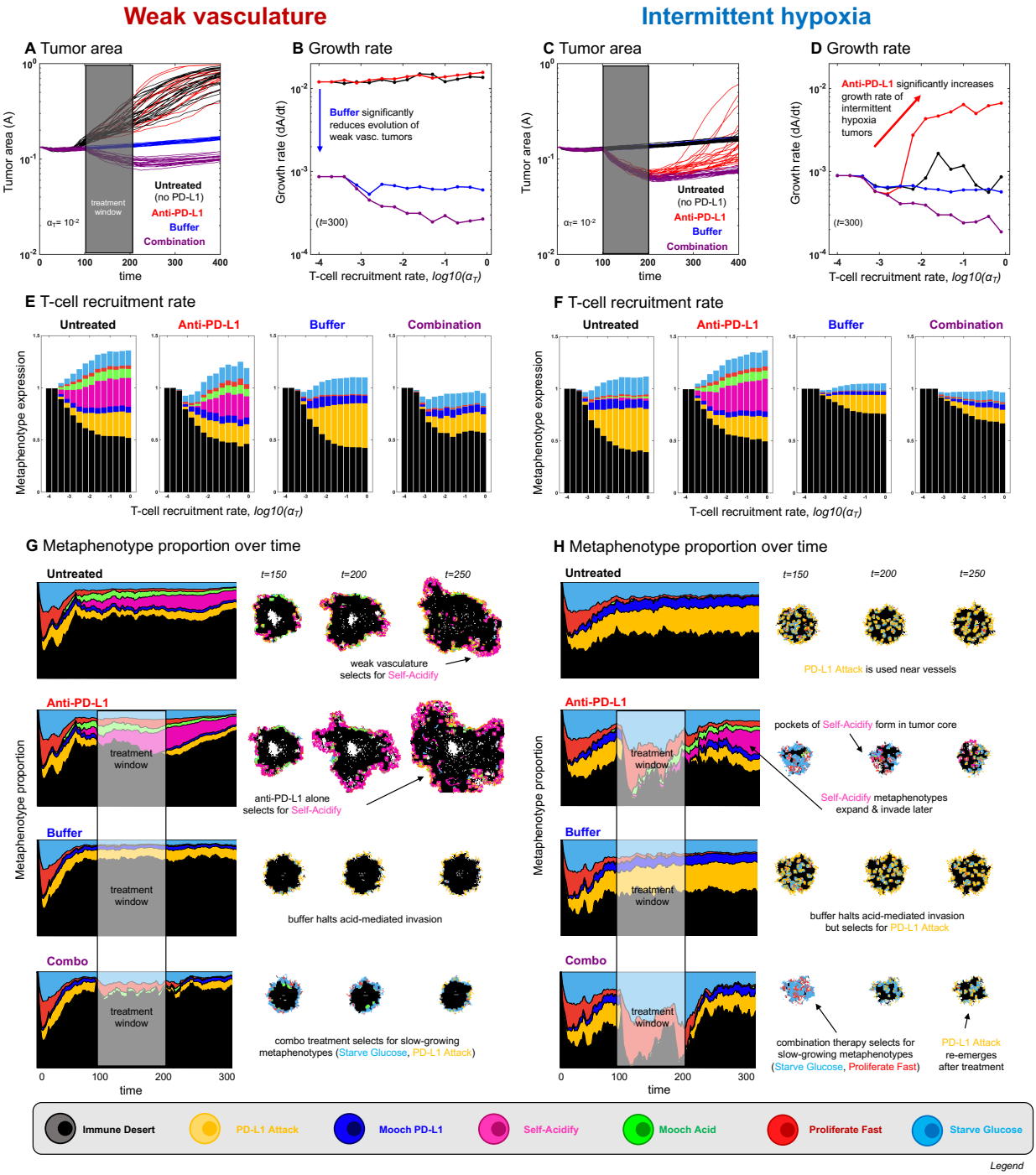

Figure 6. Evolution of metaphenotypes under treatment. Outcomes of tumor response and immune escape can be explained by observing the evolution of metaphenotypes under treatment with anti-PD-L1 (red) and buffer (blue), given in isolation or combination (purple). (A) Tumor area over time (weak vasculature) (B) growth rate over time (weak vasculature). (C) Tumor area over time (intermittent hypoxia vasculature) (D) growth rate over time (intermittent hypoxia vasculature). (E) Final distribution of metaphenotypes after treatment ($t = 300$; weak vasculature). (F) Final distribution of metaphenotypes after treatment ($t = 300$; intermittent hypoxia). (G,H) Muller plots showing the frequency of metaphenotypes over time in untreated and mono- or combination therapy, with snapshots of spatial configurations during and after treatment, with moderate immune predation ($\alpha_T = 10^{-2}$). See associated supplemental videos S2 and S3.

therapy outperforms monotherapy in both vascular settings, but vascular dynamics drive differences in monotherapy outcomes. For example, anti-PD-L1 therapy does not appreciably slow tumor evolution or growth in weak vasculature (fig. 6A,B). In contrast, anti-PD-L1 does induce large tumor remission in intermittent hypoxia (fig. 6C,D), albeit only temporarily before a strong relapse. These results are seen across a range of immune recruitment rates (fig. 6B,D).

In order to investigate the role of context-dependent selection of collective phenotypes under treatment, we define six collective phenotypes ("metaphenotypes") which act as seen in the Venn diagram in figure 5A). Each metaphenotype provides a mechanism of immune escape. The "null" metaphenotype is the lack of collective behavior: **Immune Desert** are cells which do not interact with T-cells. Next, we quantify two PD-L1 metaphenotypes: a counter-attack (tumor cell with high PD-L1 expression that has recently interacted with a T-cell; **PD-L1 Attack**, yellow), and a mooching PD-L1 (**Mooch PD-L1**, blue). As seen in figure 5B, **PD-L1 Attack** is high in cells with high PD-L1 expression while **Mooch PD-L1** is high in cells with low PD-L1 expression, but with neighbors that are high in **PD-L1 Attack**. See Box 2, equations 16 and 17. Two metaphenotypes rely on acid-inactivation: self-acidifying (highly glycolytic cells which secrete acid; **Self-Acidify**, pink) and non-producers (reside in acidic niche but do not produce acid; **Mooch Acid**, green). As seen in figure 5C, **Self-Acidify** is high in cells with a high glycolytic phenotype, hence high acid production (see 18). In contrast, **Mooch Acid** cells have low glycolytic phenotype (not producing acid) but reside in highly a acidic niche that inactivates T-cells (figure 5D). See Box 2, equations 19 and 20. We also consider a proliferative phenotype that has recently divided into empty space (**Proliferate Fast**; red). See Box 2, equations 21. Tumor cells also compete with immune cells for glucose (**Starve Glucose**; light blue). Figure 5E illustrates that **Starve Glucose** reside in areas with a high probability that T-cells die due to low glucose concentration. See Box 2, equations 22. Importantly, each of these metaphenotypes (excluding **Immune Desert**) is contingent on a recent tumor-immune interaction, allowing us to track *effective* collective phenotypes: only metaphenotypes which survive an immune interaction.

Panels E and F of figure 6 show the average metaphenotype expression (across all tumor cells) for each treatment scenario. Metaphenotype expression is defined on the interval $\texttt{MP} \in [0, 1]$ for each metaphenotype (see Methods, Box 2). Therefore, if average expression is above 1, the tumor is strongly immune resistant; on average there is more than one immune escape strategy per cell.

In all cases, the dominant metaphenotype is **Immune Desert**, representing tumor cells that have not recently interacted with a T-cell due to lack of immune infiltration, possibly from low vascularization or shielding effects from neighboring cancer cells. Vascularization drives differential selection of metaphenotypes in baseline untreated dynamics. Weak vasculature is associated with acidification metaphenotypes (**Self-Acidify**, pink; **Mooch Acid**, green). These are aggressive, highly glycolytic metaphenotypes that facilitate acid-mediated invasion. In contrast, intermittent hypoxia selects for PD-L1-based immune-escape mechanisms (**PD-L1 Attack**, yellow; **Mooch PD-L1**, dark blue).

Anti-PD-L1 selects for acidification metaphenotypes (self-acidify or mooch acid) in both vascularization cases. In contrast, buffer treatment eliminates the emergence of both **Self-Acidify** and **Mooch Acid** phenotypes by slowing evolution (e.g. refer to fig. 3C). But in response, **PD-L1 Attack** is selected (yellow). Combination therapy strongly targets acidification metaphenotypes and weakly targets PD-L1 phenotypes, leaving only less aggressive metaphenotypes (**Starve Glucose**, **Immune Desert**). Tracking the response of metaphenotypes to treatment explains why combination therapy is ideal for minimizing tumor growth, compared to monotherapy options.

2.4 Spatial configuration of metaphenotypes under treatment

The explanatory power of these defined metaphenotypes is seen most clearly by observing their spatial arrangement under high immune predation (see figure 6G,H and associated Supplemental Videos S1 and S2).

For example, weak vasculature (fig. 6G) is associated with the **Self-Acidify** and **PD-L1 Attack** metaphenotypes on the invasive front of the tumor. Much of the tumor interior is unaffected by immune cells (**Immune Desert**), regardless of tumor phenotype. Treatment with Anti-PD-L1 selects for the aggressive **Self-Acidify** metaphenotype, while Buffer selects for **PD-L1 Attack** on the tumor rim. Combination therapy is required to achieve maximum tumor response, resulting in small tumors consisting mostly of non-aggressive metaphenotypes (**Starve Glucose** or **Proliferate Fast**).

In contrast, under intermittent hypoxia vasculature the **Immune Desert** comprises a much lower fraction

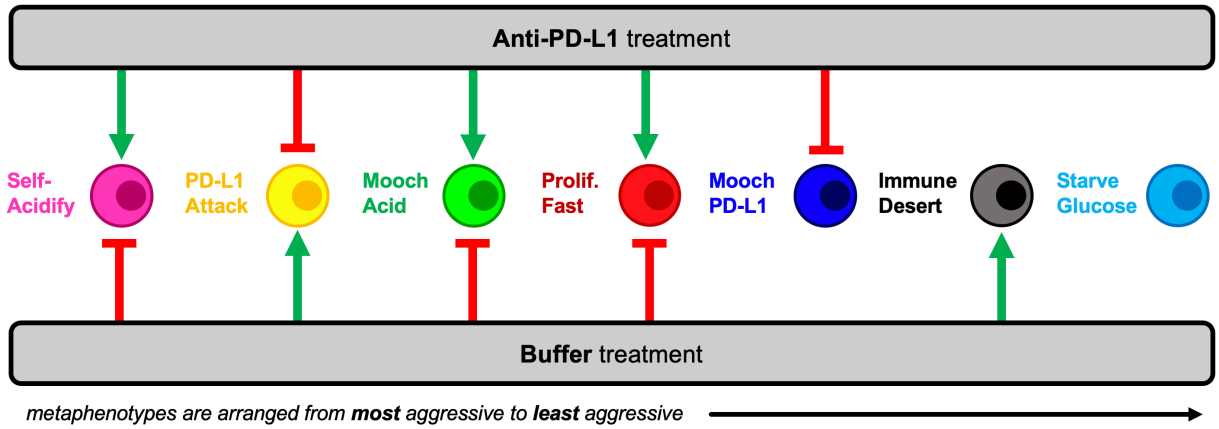

Figure 7. Summary schematic. Each metaphenotype is ordered from most aggressive to least aggressive in facilitating acid-mediated invasion and tumor growth under immune predation. This interaction diagram describes the role of two treatments (anti-PD-L1, buffer) in promoting (green) or inhibiting (red) each metaphenotype. Metaphenotypes names are shown on the left, and defined mathematically in Box 2. Broadly, the two treatments offset one another by inhibiting the metaphenotypes that the opposite treatment promotes.

of tumor metaphenotypes, as this improved vascularization delivers T-cells into the tumor core. **PD-L1 Attack** is used near blood vessels and on the tumor rim, and **Self-Acidify** does not occur due to low turnover in untreated conditions. Treatment with Anti-PD-L1 negates immune escape from **PD-L1 Attack**, inducing cellular turnover and subsequently selecting for **Self-Acidify** and **Mooch Acid** metaphenotypes. Combination therapy results in small, slow-growing tumors with less aggressive metaphenotypes (**Mooch PD-L1** and **Starve Glucose**).

In both vasculature settings, cells slightly inset from the rim use metaphenotypes that **Mooch Acid** and **Mooch PD-L1** from cells on the rim (see Supplemental Videos S1 and S2) while cells in regions of high turnover employ the **Proliferate Fast** metaphenotype. **Starve Glucose** remains at low levels throughout all treatment modalities and vasculature settings. As seen in the supplemental videos (S1 and S2), it is difficult to determine the major driver of immune escape from the maps of phenotypes alone, as areas of high glycolysis and high PD-L1 are each spatially heterogeneous and overlapping.

3 Discussion

The importance of acidity in modulating immune response in cancer is only just beginning to be understood. Our results highlight the potential utility in buffering agents combined with immunotherapy. Whilst such agents are not currently used in cancer treatment there is a growing body of evidence that more alkaline diets can facilitate standard cancer treatments. Patient compliance with sodium bicarbonate has been an an issue in previous clinical trials due to GI irritability, leading to an investigation of dietary intake of highly buffered foods or supplements[58]. The exact mechanism of action is as yet to be understood but previous work has shown how acid-mediated invasion can be modulated through diet changes[58]. Several factors contribute to a lack of responsiveness to immune checkpoint blockers, including abnormal tumor microenvironment where poor tumor perfusion hinders drug delivery and increases immunosuppression[59]. Poor vascularization also leads to a hypoxic and therefore acidic microenvironment, increasing immunosuppression. The modeling above recapitulates this trend, as immune predation is less effective in weak vascularized tumors than in intermittently vascularized tumors. Vascular renormalization can be enhanced through administration of anti-angiogenic agents (e.g., anti-vascular endothelial growth factor agents) to fortify immature blood vessels and improve tumor perfusion[60]. However, our results indicate that administration of immune checkpoint blockade in tumors with increased vascularization may lead to a short-term good response but poor long-term outcomes as selection for increased glycolysis occurs. Mathematical modeling allows for direct comparison of initially identical simulations in the absence (figure 3) and presence (figure 4) of immune predation. We observe an immune gambit under high vascular renewal (intermittent hypoxia), due to an evolutionary

bottleneck. The impact of this evolutionary bottleneck is reduced when anti-PD-L1 is combined with buffer therapy.

Characterization of collective phenotypes into metaphenotypes enables a straightforward explanation of the effect of treatment in a complex, multi-scale model. This characterization is necessary, in part, due to the fact that acid-mediated invasion is a collective phenotype phenomenon (figure 1). Immune escape is also, by definition, a collective phenomenon by requiring the presence of two cell types in close proximity: tumor and immune. A summary schematic of the results is shown in figure 7. The interaction diagram describes the role of anti-PD-L1 and buffer in either promoting (green) or inhibiting (red) each metaphenotype. Broadly, the two treatments offset one another by inhibiting the metaphenotypes that the opposite treatment promotes. The two exceptions, starve glucose and immune desert, are both non-aggressive phenotypes. This summary schematic illustrates the utility of defining metaphenotypes in the context of treatment to provide insight into immune-escape dynamics. The most dominant mechanism of immune escape seen in the model is the lack of immune interactions (immune desert), especially when the tumor bed is poorly vascularized. Tumor-expressed PD-L1 is a viable immune-escape mechanism in the absence of treatment, across a range of vascularization, but treatment with anti-PD-L1 selects for the two acid-inactivation metaphenotypes (**Self-Acidify** and **Mooch Acid**). Environmental conditions must also consider neighboring (and self) cellular phenotypes. A cell in acidic conditions may rely on acid-inactivation either by self-production of acid or mooching from neighboring producer cells, a form of "public good"[61]. Buffer therapy limits selection for self-acidification, driving selection toward less aggressive metaphenotypes (**Glucose Starvation** or **Immune Desert**). It's also important to note that mooching metaphenotypes only occur in the presence of non-mooching phenotypes. Because of this, and the fact that phenotypes of individual cells change only slowly (upon division), mooching phenotypes are not expected to be a viable long-term immune escape strategy, but limited to transient, local patches co-localized with non-moochers. However, in a model where the ratio of two phenotypes is determined stochastically, for example, a population of both phenotypes could coexist for a longer period of time.

The intimate feedback between a growing tumour and the homeostatic tissue its invading drives both ecological and evolutionary dynamics that should not be ignored in modern cancer therapy. The results we presented here indicate that treatments that modulate context may turn out to be just as important as those that target the tumour.

4 Methods

The mathematical model here builds on an experimentally validated hybrid discrete-continuum multiscale model of cancer metabolism that incorporates the production of acid and acquired resistance to extracellular pH[8–10,62]. The model includes three diffusible molecules (oxygen, protons, glucose), four cellular automata agents (tumor cells, normal cells, immune cells, and blood vessels), and two treatments (anti-PD-L1 immunotherapy and a pH buffer such as sodium bicarbonate).

4.1 Model Parameterization

Values for parameterization are shown in Table 1. Values for parameters are typically identical to previous publications using the non-immune metabolism model[8,9], except where parameter values are shown in brackets. In these cases, a parameter sweep is performed across the full range in order to determine the effect of the parameter on outcomes and test hypotheses. New parameters developed in this manuscript (i.e. the immune module) are shown below the solid line.

Table 1. Model Parameterization

Parameters	Value	Units	Description
δx	20	μm	Diameter of CA grid point
p_D	0.005	1/d	Normal tissue death rate
p_Δ	0.7	1/d	Death probability in poor conditions
p_n	5e-4	1/d	Necrotic turnover rate
D_O	1820	$\mu m^2/s$	Diffusion rate of oxygen
D_g	500	$\mu m^2/s$	Diffusion rate of glucose
D_H	1080	$\mu m^2/s$	Diffusion of protons
O_O	0.0556	mmol/L	Oxygen concentration in blood
G_O	5	mmol/L	Glucose concentration in blood
pH_O	7.4	pH	pH of blood
V_O	0.012	mmol/L/s	Maximal oxygen consumption
k_O	0.005	mmol/L	Half-max oxygen concentration
k_G	0.04	mmol/L	Half-max glucose concentration
k_H	2.5e-4	-	Proton buffering coefficient
A_d	0.35	-	ATP threshold for death
A_q	0.8	-	ATP threshold for quiescence
$p_{H,min}$	6.1	pH	Maximal acid resistance phenotype
$p_{H,norm}$	6.65	pH	Normal acid resistance phenotype
ΔH	0.003	pH	Phenotype variation rate (acid res.)
$p_{G,max}$	50	-	Maximal glycolytic phenotype
ΔG	0.15	-	Phenotype variation rate (glycolysis)
τ_{min}	0.95	Days	Minimum cell cycle time
σ_{min}	80	μm	Minimum vessel spacing
σ_{mean}	150	μm	Mean vessel spacing
v_{mean}	[5, 100]	Days	Vessel stability
p_{ang}	[0, 1]	-	Angiogenesis rate
T_M	1	-	Probability T-cell moves
τ_T	4	-	T-cell response delay
α_T	[1e-4,1e-1]	-	T-cell recruitment rate
β_T	10	Days	Non-activated T-cell decay
$p_{P,min}$	5	-	Maximal PD-L1 phenotype
$p_{P,norm}$	2.7	-	Normal PD-L1 phenotype
ΔP	[0,1]	-	Phenotype variation rate (PD-L1)
d_e	0.042	Days	T-cell engagement duration
H_e	6.6	-	half-max pH T-cell engagement time
σ_e	4	-	steepness of T-cell engagement time
H_p	6.6	-	half-max pH T-cell engagement probability
σ_p	6	-	steepness of T-cell engagement probability
L_i	65.35	percent	T-cell survival rate in high glucose
L_0	21.78	percent	T-cell survival rate in low glucose
L_g	-16.67	percent	T-cell glucose deprivation parameter
D_A	100	$\mu m^2/s$	Anti-PD-L1 diffusion parameter
γ_A	0.5	$1/s$	Anti-PD-L1 natural decay rate
γ_P	0.001	$1/s$	Cellular bound PD-L1 decay rate

5 Box 1: Methods

5.1 Baseline mathematical model

An overview of the mathematical model is shown in figure 2. The model simulates a two-dimensional slice through a tumor via a coupled cellular automata (CA) and partial differential equation (PDE) model. Vasculature is modeled as a set of point sources, with spacing consistent with those measured in normal stroma[8]. As timescales of metabolism and cell-scale dynamics (e.g. proliferation) vary significantly, we solve the PDEs to reach steady state between CA timesteps. The model includes several diffusible molecules: oxygen, acid, and glucose (figure 2A, yellow boxes). The concentration of each diffusible is modeled by the following diffusion-production-consumption equation:

$$\frac{\partial C}{\partial t} = D\nabla^2 C + f(x,t) \tag{1}$$

where C represents the diffusible molecule concentration, D is the diffusion constant, and $f(x,t)$ is the molecule-specific rate of consumption/production of each particular molecule. For example, oxygen consumption (f_O) by cells is given by Michaelis-Menten dynamics:

$$f_O = -V_O \frac{O}{O + k_O} \tag{2}$$

where k_O is the oxygen concentration for half-maximal oxygen consumption and V_O is the maximal oxygen consumption by cells. Glucose consumption is given by the following modified Michaelis-Menten equation:

$$f_G = -\left(\frac{p_G A_o}{2} + \frac{27 f_O}{10}\right)\frac{G}{G + k_G} \tag{3}$$

where p_G is the heritable trait which represents aerobic glycolysis and its resultant excessive glucose consumption. A_o is the ATP production rate in normal cells, k_G is glucose concentration for half-maximal glucose consumption. ATP production rate is given by:

$$f_A = -\left(2 f_G + \frac{27 f_O}{5}\right), \tag{4}$$

and proton production rate given by:

$$f_H = k_H\left(\frac{29(p_G V_O + f_O)}{5}\right). \tag{5}$$

5.2 Phenotypic drift

Both normal and tumor cells undergo a decision process in figure 2B, involving cell cell cycle dynamics, proliferation and phenotypic drift. Cells with low ATP efficiency or cells which are maladapted for acidosis die. Cells take on three phenotypic traits: acid resistance (p_H), glycolysis (p_G), PD-L1 expression (p_P). Phenotypes may drift upon cell division as follows:

$$p_i(t + \Delta t) = p_i(t) \cdot (1 + \Delta_i)^{(U(-1,1))} \tag{6}$$

where $i \in \{H, G, P\}$, representing acid-resistance, glycolysis, PD-L1 phenotypes respectively (see Table 1). $U(-1,1)$ represents a uniform probability distribution drawn on the interval -1 to 1 and Δt is the timestep (2 hours). Phenotype variation rate parameters ($\Delta_i \in [\Delta_G, \Delta_H, \Delta_P]$) are shown in Table 1.

5.3 Immune recruitment model

Immune cells are recruited in proportion to the current tumor size a few days prior, $N(t-\tau_T)$) at a rate α_T until the number of T-cells equals or exceeds this value. T-cells undergo a natural decay rate if they have not encountered a tumor cell in the past β_T number of days.

$$T(t+1) = \begin{cases} \alpha_T N(t-\tau_T) - \frac{1}{\beta_T} T(t), & N(t-\tau_T) > T(t) \\ T(t) - \frac{1}{\beta_T} T(t), & N(t-\tau_T) \leq T(t) \end{cases} \tag{7}$$

Tumor cells have several mechanisms for immune evasion in the mathematical model: PD-L1 and acid inactivation.

5.4 PD-L1

The probability, P_k, that a tumor cell is successfully eliminated by a T-cell is a function of the constitutive PD-L1 expression (p_P) and the bound PD-L1 (p_B; see section on treatment with anti-PD-L1 below):

$$P_k = 1 - \frac{10^{p_P - p_B}}{10^{p_{P,norm} - p_{P,min}}} \tag{8}$$

where $p_{P,min}$ and $p_{P,norm}$ are the maximal PD-L1 phenotype (corresponding to zero probability of kill; see figure 5B) and normal PD-L1 phenotype, respectively. See table 1 for parameter values.

5.5 T-cell viability in high acid

Recent results from Pilon-Thomas et. al. have suggested that acid does not affect T-cell viability but instead impairs activation[26]. Low pH arrests T-cell cytokine and chemokine production (a measure of activation) . Thus, we model probability of successful engagement of a cancer cell by a T-cell depends on the microenvironmental pH:

$$P_e = \frac{1}{1 + e^{-\sigma_p (H - H_p)}} \tag{9}$$

where H is the pH value, H_p is the half-max engagement probability and σ_p represents the pH at which engagement probability is half its maximum value. Secondly, exocytosis of lytic granules is impaired in low pH[63], causing increased time to kill targets in low pH. The probability that a tumor cell successfully inactivates a T-cell due to low acid is given by:

$$P_{AI} = 1 - \frac{P_e \Delta t}{d_e \left(1 + e^{-\sigma_e (H - H_e)}\right)} \tag{10}$$

where d_e represents the minimum engagement time duration, modulated by acid concentration, H[64]. H_e is the half-max engagement time and σ_e is the steepness parameter, and Δt is the length of a single time step (2 hours).

T-cells are also assumed to undergo death at higher rates in low glucose concentrations. This component of the model was parameterized using experimental data from ref. 57, where probability of death after two days is fit to the following equation:

$$L(G) = (L_0 - L_i) e^{G L_g} + L_i, \tag{11}$$

where L_0 and L_i T-cell survival rate in low and high glucose concentrations, G, with steepness parameter L_g (see figure 5E).

5.6 Immune susceptibility

The total immune susceptibility of a cell is the likelihood of a T-cell kill as a function of PD-L1 expression multiplied by the likelihood that a T-cell is not acid-inactivated:

$$S = P_k(1 - P_{AI}), \tag{12}$$

5.7 Treatment

Two treatments are considered: anti-PD-L1 and buffer therapy. Anti-PD-L1 is modelled as a diffusible molecule (eqn. 1), with tumor cell uptake of bound PD-L1 (p_B) at rate D_A and natural decay at rate γ_A (see Table 1). Bound PD-L1 in each tumor cell is limited to the range $p_B \in [0, p_P]$, where T-cell kill rate, P_K, is a function of the difference between constitutively expressed and bound PD-L1 (see figure 5B). Cell internal bound PD-L1 decays at rate γ_P. Buffer therapy is modeled as a change in proton buffering coefficient, k_H:

$$k_H = 0.00025(1 - B(t)), \tag{13}$$

where $B(t)$ is the time-dependent administration of buffer therapy, and the baseline value of the buffering coefficient is $k_H = 0.00025$ (see Table 1 and ref. 8).

5.8 Local Neighborhoods

The model is carried out on a two-dimensional lattice where each tumor, normal, or immune cell occupies a single lattice location, (x, y). The cell's local neighborhood is a set of lattice locations defined in relation to the focal cell's location, defined as N_m ($N_m = 8$ for a Moore neighborhood). When the focal cell undergoes division a daughter cell is placed in a random neighboring grid point and the parent cell remains on the original lattice point. The cell may undergo apoptosis (death) and is removed from the domain. After each generation cells are shuffled and iterate through in random order in future time steps.

6 Box 2: Defining metaphenotypes

Let $T(x,y)$ be a two-dimensional grid representing the time since the last T-cell interaction has occurred within the local neighborhood of grid location (x,y). We define the tumor-immune interaction grid, $I(x,y)$, where $I=1$ if an immune cell has traversed within a cancer cell's neighborhood within the previous T_w days and $I=0$ otherwise at the current timestep, t.

$$I(x,y) = \begin{cases} 1, & \text{if } T(x,y) \geq t - T_w \\ 0, & \text{otherwise} \end{cases} \tag{14}$$

Metaphenotypes (MP) are defined in such a way that MP expression is scaled from zero to one and each cell can take on multiple MP: $\vec{M} = \{m_1, m_2, \ldots, m_7\}$ where $m_i \in [0,1]$

6.0.1 MP1: Immune Desert

We first consider the absence of immune interaction: the immune desert metaphenotype, MP1:

$$\texttt{MP1}(x,y) = 1 - I(x,y) \tag{15}$$

6.0.2 MP2: PD-L1 Attack

Next, we classify cells which employ the PD-L1 counter-attack, defined as high PD-L1 expression (low probability of T-cell kill; see equation 8) with a recent T-cell interaction:

$$\texttt{MP2}(x,y) = \underbrace{(1-P_k)}_{\text{Prob. avoiding T-cell kill}} \times \underbrace{I(x,y)}_{\text{recent T-cell interaction}} \tag{16}$$

6.0.3 MP3: Mooch PD-L1

In contrast to MP2, cells which interact with T-cells but have low PD-L1 expression can rely on ("mooch") neighboring cell protection. Here, the metaphenotype is proportional to neighborhood PD-L1 expression.

$$\texttt{MP3}(x,y) = \underbrace{P_k}_{\text{Prob. T-cell kill}} \times \underbrace{1 - I(x,y)}_{\text{no T-cell interactions}} \times \max_{j \in N_m} \texttt{PD-L1}_j \tag{17}$$

where N_m is a Moore neighborhood of $N_m = 8$ neighbors.

6.0.4 MP4: Self-Acidify

As cell increase glycolytic capacity (phenotype value p_G), more protons are added. The per cell proton production rate is given by:

$$p_R = f_H(1 - B(t)) \tag{18}$$

where proton production (see Methods eqn. 5) is scaled by buffer treatment concentration, $B(t)$.

$$\texttt{MP4}(x,y) = \underbrace{P_{AI}(x,y)}_{\text{Probability of Acid-Inactivation}} \times \underbrace{\bar{p}_R}_{\text{scaled proton production rate}} \times \underbrace{I(x,y)}_{\text{recent T-cell interaction}} \tag{19}$$

where the production rate, $\bar{p}_R$, is normalized such that any value for phenotype above the buffering capability of a vessel is assumed to be mostly self-acidify metaphenotype (MP4), while below is assumed to be mostly mooch acid (MP5).

6.0.5 MP5: Mooch Acid

Similarly, the mooch acidify metaphenotype occurs when the probability of T-cell acid-inactivation is high, but where the highly acidic microenvironment is not due to self-acidification.

$$\texttt{MP5}(x,y) = \underbrace{P_{AI}(x,y)}_{\text{Probability of Acid-Inactivation}} \times \underbrace{(1-\bar{p}_R)}_{\text{scaled proton production rate}} \times \underbrace{I(x,y)}_{\text{recent T-cell interaction}} \tag{20}$$

This metaphenotype typically occurs early in simulations in empty regions without tumor or vasculature.

6.0.6 MP6: Proliferate Fast

$$\texttt{MP6}(x,y) = \left(1 - \underbrace{\frac{D_{x,y}}{T_m}}_{\text{fraction of cell cycle completed}}\right) \times \underbrace{I(x,y)}_{\text{recent T-cell interaction}} \tag{21}$$

where D_i is the time until next division for the cell at location (x,y) and T_m is the inter-mitotic cell division time for a metabolically normal cell.

6.0.7 MP7: Starve Glucose

Tumor cells may also compete with T-cells to starve immune cells of glucose, giving rise to the following metaphenotype:

$$\texttt{MP7}(x,y) = \underbrace{P_g}_{\text{Prob. T-cell dies in low glucose}} \times \underbrace{I(x,y)}_{\text{recent T-cell interaction}} \tag{22}$$

Supplemental Information

Figure S1 Supplemental Video S1.mov Simulation of the full multi-scale hybrid cellular automata model: tumor spatial map, phenotypes, vascular renewal probability, T-cells, diffusible molecules (oxygen, glucose, pH), tumor cell PD-L1, and immune susceptibility (see equation 12). Each grid has corresponding colorbar (right) with marker indicating average value. This is an example realization of "weak vasculature" ($v_{mean} = 20; p_{ang} = 0.1$). Acidic conditions in tumor core select for acid resistant and glycolytic Warburg phenotype (pink color on the Tumor grid). Subsequently, nectrotic cells form in the tumor interior. Immune response is weak ($\alpha_T = 10^{-3}$), not selecting for PD-L1 positivity. The primary means of immune escape is acid-inactivation of T-cells caused by acid-producing Warburg cells.

Figure S2 Supplemental Video S2.mov Evolution of metaphenotypes in **Weak** vasculature under high immune predation ($\alpha_T = 10^{-2}$). The left-hand side shows three phenotypes (Acid Resistance, Glycolsis, and PD-L1), along with acid concentration and T-cell location. It is difficult to determine the major driver of immune escape from the maps of phenotypes alone: areas of high glycolysis and high PD-L1 are each spatially heterogeneous and overlapping. However, metaphenotypes give a detailed picture of immune escape dynamics. Much of the tumor interior is unaffected by immune cells (**Immune Desert**), regardless of tumor phenotype. The outer rim is immune-protected by **PD-L1 Attack** and **Self-Acidify** phenotypes. Slightly inset from the rim, cells use metaphenotypes that **Mooch Acid** and **Mooch PD-L1** from cells on the rim. Cells in regions of high turnover employ the **Proliferate Fast** metaphenotype. **Starve Glucose** remains at low levels throughout all treatment modalities. Treatment with Anti-PD-L1 selects for the aggressive **Self-Acidify** metaphenotype, while Buffer selects for **PD-L1 Attack**. Combination therapy results in small, slow-growing tumors with less aggressive metaphenotypes (**Mooch PD-L1** and **Starve Glucose**).

Figure S3 Supplemental Video S3.mov Evolution of metaphenotypes in **Intermittent Hypoxia** vasculature under high immune predation ($\alpha_T = 10^{-2}$). The left-hand side shows three phenotypes (Acid Resistance, Glycolsis, and PD-L1), along with acid concentration and T-cell location. Similar to S2, it is difficult to determine the major driver of immune escape from the maps of phenotypes alone: areas of high glycolysis and high PD-L1 are each spatially heterogeneous and overlapping, but metaphenotypes give a detailed picture of immune escape dynamics. Here, **Immune Desert** comprises a much lower fraction of tumor metaphenotypes, as better vascularization delivers T-cells into the tumor core. **PD-L1 Attack** is used near blood vessels and on the tumor rim, with **Mooch PD-L1** employed by nearby cells. In untreated conditions, **Self-Acidify** does not occur due to low turnover. However, Anti-PD-L1 negates immune escape from **PD-L1 Attack**, inducing turnover and selecting for **Self-Acidify** and **Mooch Acid** metaphenotypes. Combination therapy results in small, slow-growing tumors with less aggressive metaphenotypes (**Mooch PD-L1** and **Starve Glucose**).

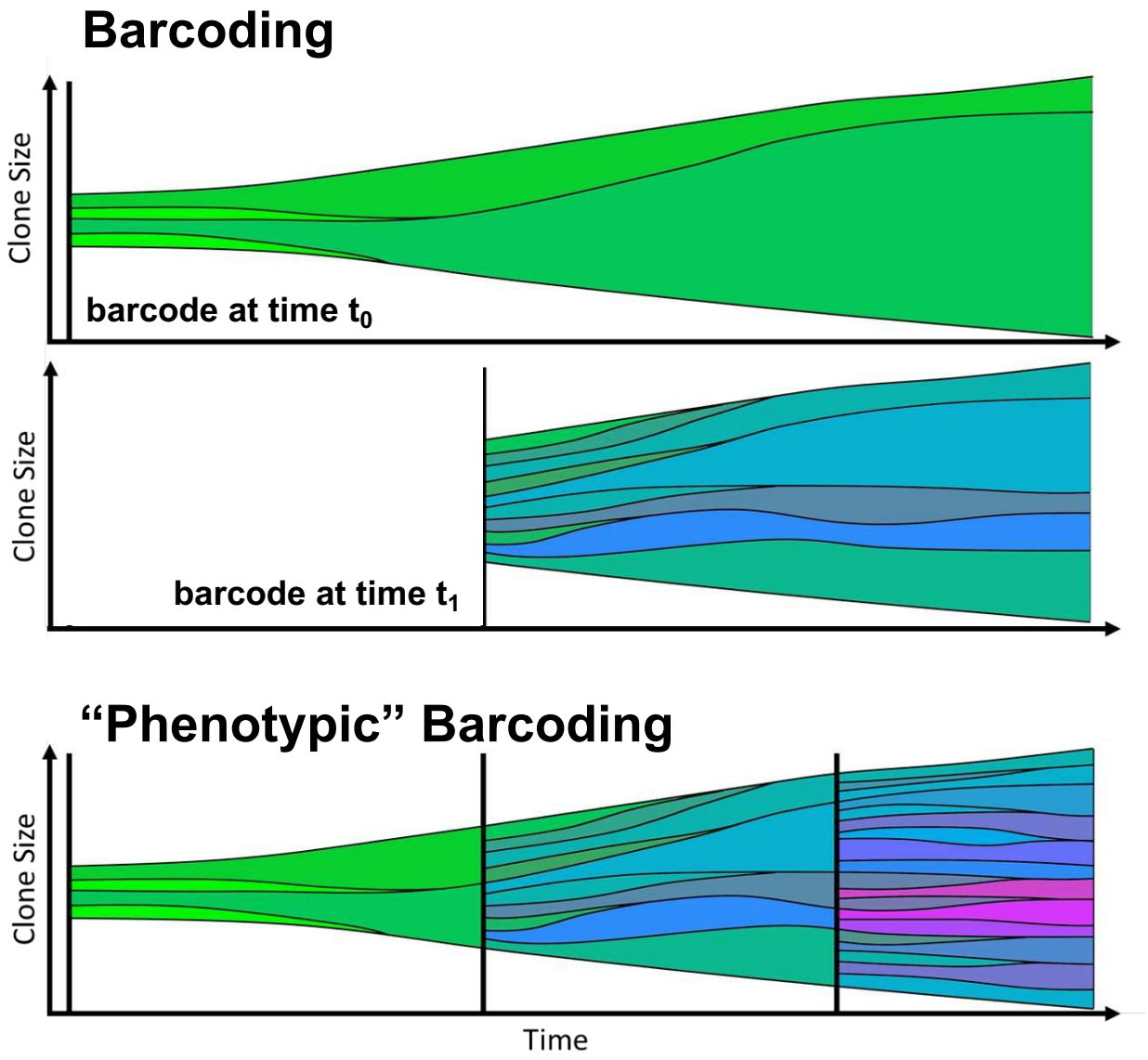

Figure S4. Phenotypic barcoding Schematic of "phenotypic barcoding" scheme for visualizing tumor evolution. At time point 0, all cells are given a unique ID, also known as a barcode (top). This can be repeated at later times (e.g., time point t1) by adding a second unique ID to each extant cell (middle). Clones and subclones can be re-colored by average phenotype (bottom) so that both the phenotype and lineage information are visualized during tumor evolution.

Acknowledgments

The authors gratefully acknowledge funding by the National Cancer Institute via the Cancer Systems Biology Consortium (CSBC) U01CA232382, the Physical Sciences Oncology Network (PSON) U54CA193489, and support from the Moffitt Center of Excellence for Evolutionary Therapy.

Author Contributions

ARAA and MRT conceived the research questions and model design. KAL contributed to model design. JW, FR, RB, and CA performed the modeling and analyses. All authors contributed to writing and editing the manuscript.

References

1. Warburg, O. Uber den stoffwechsel der karzinomezellen. *Biochem Z* **152**, 309–344 (1924).
2. Gatenby, R. A. & Gawlinski, E. T. The glycolytic phenotype in carcinogenesis and tumor invasion: insights through mathematical models. *Cancer Research* **63**, 3847–3854 (2003).
3. Gatenby, R., Gawlinski, E., Gmitro, A., Kaylor, B. & Gillies, R. Acid-mediated tumor invasion: a multidisciplinary study. *Cancer Res.* **66**, 5216 (2006).
4. Estrella, V. *et al.* Acidity generated by the tumor microenvironment drives local invasion. *Cancer Res.* **73**, 1524–1535 (2013).
5. Smallbone, K., Gatenby, R., Gillies, R., Maini, P. & Gavaghan, D. Metabolic changes during carcinogenesis: potential impact on invasiveness. *J. Theor. Biol.* **244**, 703–713 (2007).
6. Silva, A. S., Yunes, J. A., Gillies, R. J. & Gatenby, R. A. The potential role of systemic buffers in reducing intratumoral extracellular ph and acid-mediated invasion. *Cancer Research* **69**, 2677–2684 (2009).
7. Martin, N. K., Gaffney, E. A., Gatenby, R. A. & Maini, P. K. Tumour–stromal interactions in acid-mediated invasion: a mathematical model. *Journal Theoretical Biology* **267**, 461–470 (2010).
8. Robertson-Tessi, M., Gillies, R. J., Gatenby, R. A. & Anderson, A. R. Impact of metabolic heterogeneity on tumor growth, invasion, and treatment outcomes. *Cancer Research* **75**, 1567–1579 (2015).
9. Ibrahim-Hashim, A. *et al.* Defining cancer subpopulations by adaptive strategies rather than molecular properties provides novel insights into intratumoral evolution. *Cancer Research* **77**, 2242–2254 (2017).
10. Damaghi, M. *et al.* The harsh microenvironment in early breast cancer selects for a warburg phenotype. *Proceedings National Academy Sciences* **118** (2021).
11. Bravo, R. R. *et al.* Hybrid automata library: A flexible platform for hybrid modeling with real-time visualization. *PLOS Computational Biology* **16**, 1–28 (2020).
12. Makowski, L., Chaib, M. & Rathmell, J. C. Immunometabolism: From basic mechanisms to translation. *Immunological Reviews* **295**, 5–14 (2020).
13. Purohit, V., Wagner, A., Yosef, N. & Kuchroo, V. K. Systems-based approaches to study immunometabolism. *Cellular & Molecular Immunology* 1–12 (2022).
14. Kuznetsov, V., Makalkin, I., Taylor, M. & Perelson, A. Nonlinear dynamics of immunogenic tumors: Parameter estimation and global bifurcation analysis. *Bull. Math. Biol.* **56**, 295–321 (1994).
15. Kirschner, D. & Panetta, J. Modeling immunotherapy of the tumor-immune interaction. *J. Math. Biol.* **37**, 235–252 (1998).
16. de Pillis, L., Radunskaya, A. & Wiseman, C. A validated mathematical model of cell-mediated immune response to tumor growth. *Cancer Res.* **65**, 7950 (2005).
17. Mallet, D. G. & De Pillis, L. G. A cellular automata model of tumor–immune system interactions. *Journal Theoretical Biology* **239**, 334–350 (2006).
18. Robertson-Tessi, M., El-Kareh, A. & Goriely, A. A mathematical model of tumor–immune interactions. *Journal Theoretical Biology* **294**, 56–73 (2012).
19. Robertson-Tessi, M., El-Kareh, A. & Goriely, A. A model for effects of adaptive immunity on tumor response to chemotherapy and chemoimmunotherapy. *Journal Theoretical Biology* **380**, 569–584 (2015).
20. Bottino, D., Liu, R., Bazzazi, H. & Venkatakrishnan, K. Quantitative translation in immuno-oncology research and development. *Clinical Pharmacology & Therapeutics* .
21. Mahlbacher, G. E., Reihmer, K. C. & Frieboes, H. B. Mathematical modeling of tumor-immune cell interactions. *Journal Theoretical Biology* **469**, 47–60 (2019).
22. Norton, K.-A., Gong, C., Jamalian, S. & Popel, A. S. Multiscale agent-based and hybrid modeling of the tumor immune microenvironment. *Processes* **7**, 37 (2019).
23. Kareva, I. & Berezovskaya, F. Cancer immunoediting: a process driven by metabolic competition as a predator–prey–shared resource type model. *Journal Theoretical Biology* **380**, 463–472 (2015).

24. El-Kenawi, A. *et al.* Acidity promotes tumour progression by altering macrophage phenotype in prostate cancer. *British Journal Cancer* **121**, 556–566 (2019).

25. Wu, H. *et al.* T-cells produce acidic niches in lymph nodes to suppress their own effector functions. *Nature communications* **11**, 1–13 (2020).

26. Pilon-Thomas, S. *et al.* Neutralization of tumor acidity improves antitumor responses to immunotherapy. *Cancer Research* **76**, 1381–1390 (2016).

27. Kumagai, S. *et al.* Lactic acid promotes pd-1 expression in regulatory t cells in highly glycolytic tumor microenvironments. *Cancer Cell* (2022).

28. Chang, C.-H. *et al.* Metabolic competition in the tumor microenvironment is a driver of cancer progression. *Cell* **162**, 1229–1241 (2015).

29. Watson, M. J. *et al.* Metabolic support of tumour-infiltrating regulatory t cells by lactic acid. *Nature* **591**, 645–651 (2021).

30. Brown, J. A. *et al.* Blockade of programmed death-1 ligands on dendritic cells enhances t cell activation and cytokine production. *The Journal Immunology* **170**, 1257–1266 (2003).

31. Dong, H. *et al.* Tumor-associated b7-h1 promotes t-cell apoptosis: a potential mechanism of immune evasion. *Nature Medicine* **8**, 793–800 (2002).

32. Cai, J., Wang, D., Zhang, G. & Guo, X. The role of pd-1/pd-l1 axis in treg development and function: implications for cancer immunotherapy. *OncoTargets therapy* **12**, 8437 (2019).

33. Schreiber, R. D., Old, L. J. & Smyth, M. J. Cancer immunoediting: integrating immunity's roles in cancer suppression and promotion. *Science* **331**, 1565–1570 (2011).

34. Rosenthal, R., Swanton, C. & McGranahan, N. Understanding the impact of immune-mediated selection on lung cancer evolution. *British Journal Cancer* 1–3 (2021).

35. Mascaux, C. *et al.* Immune evasion before tumour invasion in early lung squamous carcinogenesis. *Nature* **571**, 570–575 (2019).

36. Kather, J. N. *et al.* Topography of cancer-associated immune cells in human solid tumors. *Elife* **7**, e36967 (2018).

37. Kather, J. N. & Halama, N. Harnessing the innate immune system and local immunological microenvironment to treat colorectal cancer. *British Journal Cancer* **120**, 871–882 (2019).

38. Logsdon, E. A., Finley, S. D., Popel, A. S. & Gabhann, F. M. A systems biology view of blood vessel growth and remodelling. *Journal Cellular Molecular Medicine* **18**, 1491–1508 (2014).

39. Ibrahim-Hashim, A. *et al.* Systemic buffers inhibit carcinogenesis in tramp mice. *The Journal Urology* **188**, 624–631 (2012).

40. Robey, I. F. *et al.* Bicarbonate increases tumor ph and inhibits spontaneous metastases. *Cancer research* **69**, 2260–2268 (2009).

41. Hashim, A. I. *et al.* Reduction of metastasis using a non-volatile buffer. *Clinical & experimental metastasis* **28**, 841–849 (2011).

42. Chamseddine, I. M. & Rejniak, K. A. Hybrid modeling frameworks of tumor development and treatment. *Wiley Interdisciplinary Reviews: Systems Biology Medicine* **12**, e1461 (2020).

43. Basanta, D. & Anderson, A. R. Homeostasis back and forth: an ecoevolutionary perspective of cancer. *Cold Spring Harbor Perspectives Medicine* **7**, a028332 (2017).

44. West, J., Schenck, R. O., Gatenbee, C., Robertson-Tessi, M. & Anderson, A. R. Normal tissue architecture determines the evolutionary course of cancer. *Nature Communications* **12**, 1–9 (2021).

45. Frankenstein, Z. *et al.* Stromal reactivity differentially drives tumour cell evolution and prostate cancer progression. *Nature Ecology & Evolution* **4**, 870–884 (2020).

46. Lakatos, E. *et al.* Evolutionary dynamics of neoantigens in growing tumors. *Nature Genetics* **52**, 1057–1066 (2020).

47. Williams, M. J. *et al.* Measuring the distribution of fitness effects in somatic evolution by combining clonal dynamics with dN/dS ratios. *Elife* **9**, e48714 (2020).

48. Zapata, L. *et al.* dN/dS dynamics quantify tumour immunogenicity and predict response to immunotherapy. *bioRxiv* (2020).

49. Hammerl, D. *et al.* Spatial immunophenotypes predict response to anti-pd1 treatment and capture distinct paths of t cell evasion in triple negative breast cancer. *Nature Communications* **12**, 1–13 (2021).

50. Gong, C. *et al.* A computational multiscale agent-based model for simulating spatio-temporal tumour immune response to pd1 and pdl1 inhibition. *Journal Royal Society Interface* **14**, 20170320 (2017).

51. Gong, C., Ruiz-Martinez, A., Kimko, H. & Popel, A. S. A spatial quantitative systems pharmacology platform spqsp-io for simulations of tumor—immune interactions and effects of checkpoint inhibitor immunotherapy. *Cancers* **13**, 3751 (2021).

52. Jiménez-Sánchez, J. *et al.* Evolutionary dynamics at the tumor edge reveal metabolic imaging biomarkers. *Proceedings National Academy Sciences* **118** (2021).

53. Yeang, C.-H. & Beckman, R. A. Long range personalized cancer treatment strategies incorporating evolutionary dynamics. *Biology Direct* **11**, 56 (2016).

54. Beckman, R. A. & Yeang, C.-H. Nonstandard personalized medicine strategies for cancer may lead to improved patient outcomes. *Personalized Medicine* **11**, 705–719 (2014).

55. Hutchinson, L. Predicting cancer's next move. *Nature Reviews Clinical Oncology* **11**, 61–62 (2014).

56. Gatenbee, C. D., Schenck, R. O., Bravo, R. R. & Anderson, A. R. Evofreq: visualization of the evolutionary frequencies of sequence and model data. *BMC Bioinformatics* **20**, 1–4 (2019).

57. Jacobs, S. R. *et al.* Glucose uptake is limiting in t cell activation and requires cd28-mediated akt-dependent and independent pathways. *The Journal Immunology* **180**, 4476–4486 (2008).

58. Pilot, C., Mahipal, A. & Gillies, R. Buffer therapy—buffer diet. *J. Nutr. Food Sci* **8** (2018).

59. Munn, L. L. & Jain, R. K. Vascular regulation of antitumor immunity. *Science* **365**, 544–545 (2019).

60. Mpekris, F. *et al.* Combining microenvironment normalization strategies to improve cancer immunotherapy. *Proceedings National Academy Sciences* **117**, 3728–3737 (2020).

61. Archetti, M. & Pienta, K. J. Cooperation among cancer cells: applying game theory to cancer. *Nature Reviews Cancer* **19**, 110–117 (2019).

62. Anderson, A. R. A hybrid mathematical model of solid tumour invasion: the importance of cell adhesion. *Mathematical Medicine Biology: A Journal IMA* **22**, 163–186 (2005).

63. Mendler, A. N. *et al.* Tumor lactic acidosis suppresses ctl function by inhibition of p38 and jnk/c-jun activation. *International Journal Cancer* **131**, 633–640 (2012).

64. Rothstein, T. L., Mage, M., Jones, G. & McHugh, L. L. Cytotoxic t lymphocyte sequential killing of immobilized allogeneic tumor target cells measured by time-lapse microcinematography. *The Journal Immunology* **121**, 1652–1656 (1978).